Supplementary Information

Taming Zinc Electrodeposition from the Root to Break Zinc Utilization/Capacity Barriers in Practical Zinc Batteries

Xinhua Zheng,*[a] Bibo Han,[a] Chaofan Liu,[a] Ruilin Li,[a] Chengchao Li,[b] Shikai Liu,*[a] Faxing Wang,*[c] Yuping Wu*[c]

[a]Department of School of Materials Science and Engineering, Henan University of Technology. Zhengzhou 450001, Henan, China.

[b]Guangdong Provincial Key Laboratory of Plant Resources Biorefinery, School of Chemical, Engineering and Light Industry, Guangdong University of Technology, Guangzhou 510006, Guangdong, China.

[c]Confucius Energy Storage Lab, School of Energy and Environment & Z Energy Storage Center, Southeast University, Nanjing 211189, Jiangsu, China.

Corresponding authors: xhzheng@haut.edu.cn; shikai_liu@haut.edu.cn; faxing.wang@seu.edu.cn; wuyp@seu.edu.cn

Experimental Section

Materials

Zinc sulfate heptahydrate (ZnSO$_4$·7H$_2$O, National Pharmaceutical Group Chemical Reagent Co., Ltd.), sodium sulfate (Na$_2$SO$_4$, National Pharmaceutical Group Chemical Reagent Co., Ltd.), elemental bromine (Br$_2$, Shanghai Macklin Biochemical Technology Co., Ltd.), zinc bromide (ZnBr$_2$, Shanghai Macklin Biochemical Technology Co., Ltd.), tetrapropylammonium bromide (TPABr, Shanghai Macklin Biochemical Technology Co., Ltd.), Polyethylene oxide (PEO, Hefei Qiansheng Biotechnology Co., Ltd.), acetonitrile (C$_2$H$_3$N, National Pharmaceutical Group Chemical Reagent Co., Ltd.), Ketjenblack EC-600JD conductive carbon (Zhengzhou Jinghong Battery Materials Co., Ltd.), GF/B glass fiber separator (100 μm thickness, Whatman), Zn foil (200 μm, Beijing Xinruichi Technology Co., Ltd.), Cu foil (50 μm, Beijing Xinruichi Technology Co., Ltd.), brass foil (100 μm, Beijing Xinruichi Technology Co., Ltd.), Ti foil (50 μm, Beijing Xinruichi Technology Co., Ltd.), and carbon felt (30 g m^{-2}, Dalian Longtian Technology Co., Ltd.) were used in this work. It is important to note that both copper and brass substrates were first sanded with 4000 mesh SiC sandpaper, then immersed in dilute sulphuric acid to remove surface oxides and contaminants, and followed by ultrasonically-assisted cleaning in ethanol for 10 min and then blow-dried and set aside.

Characterizations

Zn deposition patterns on Cu and brass substrates were investigated using optical microscopy (HAWKEYE XJ-2) and scanning electron microscopy (SEM, JEOL-6700F). The crystal phase composition of the substrates was determined by X-ray diffraction (XRD, Smart Lab) with monochromatic Cu-Kα radiation. Elemental analysis of the Cu and brass substrates were conducted via X-ray photoelectron spectroscopy (XPS, Thermo ESCALAB 250Xi). Hydrogen generation during Zn plating was quantified used a gas chromatograph-mass spectrometer (GC-MS,

Shimadzu GC-2014). Three-dimensional surface topography and roughness parameters of Zn deposits were quantified through white light interferometry (Zegage, Zygo). Wettability characteristics of electrolytes on metallic substrates (Cu and brass) were evaluated via contact angle measurements using a DSA100 instrument (KRÜSS GmbH, Germany) at room temperature. Measurements were conducted with a constant droplet with a volume of 4 μL (2 M $ZnSO_4$ electrolyte), meanwhile the experimental were assessed at three different positions on each substrate (Cu and brass) to ensure statistical reliability. Inductively Coupled Plasma-mass Spectrometry (ICP-MS, iCAP RQ) was employed to measure the evolution of Zn^{2+} concentration in electrolyte. The pristine electrolyte consisted of 0.5 M $ZnBr_2$ + 0.25 M TPABr, while the electrolytes for ICP-MS tests were collected from $Zn-Br_2$ batteries at different cycles at an areal capacity of 1 mAh cm^{-2}. All of the electrolyte were diluted to 1000,000 times in ICP-MS measurements. The chemical composition of electrolyte retrieved from $Zn-Br_2$ batteries at different cycles were investigated through ultraviolet-visible (L5S UV-Vis, China) and Fourier-transform infrared spectroscopy (FTIR, Prestige-21). The ionic conductivity of electrolytes extracted from the $Zn-Br_2$ batteries at different cycle stages was measured using a portable conductivity meter (DDBJ-351L, China). The viscosity of the electrolytes was tested with a rotational viscometer (SNB-1, China) at a rotational speed of 60 rpm with an electrolyte volume of 30 mL.

Batteries assembly

In the half cells, Zn foil was used as the counter electrode, Cu foil and brass were used as the working electrodes, and glass fiber was used as the separator. 80 μL of 2 M $ZnSO_4$ was used as the electrolyte, and it was assembled into CR2032 coin cell for testing.

The $Zn-Br_2$ batteries were tested in a self-made plexiglass device (Fig. S26). 3 mL solution of 0.5 M $ZnBr_2$ + 0.25 M TPABr was used as the electrolyte. The cathode was a carbon felt loaded with a certain mass of $TPABr_3$, and the anode was brass with pre-deposited Zn (the capacity of pre-deposited Zn is 1.2 times the specified capacity of the test), with an effective working area of 1 cm^2.

We would like to clarify that different electrolytes were used in different tests. The electrode test of HER overpotentials and Tafel curves required no Zn^{2+} to avoid its effect on stability, thus 2 M Na_2SO_4 was used. The half-cell measurements selected a commonly used electrolyte system of 2 M $ZnSO_4$, which was compared well with previous work. While 0.5 M $ZnBr_2$ + 0.25 M TPABr in the $Zn-Br_2$ battery was to provide the necessary active substance and complexing agent for the cathode and anode. On the cathode side, we mixed $TPABr_3$, ketjen black-EC600JD, and PEO in an acetonitrile solvent with a mass ratio of 8:1:1 to make a uniform slurry. The slurry was dropped onto the carbon felt and then dried in an oven at 70 °C. Specifically, in the battery cathode with a capacity of 5 mAh cm^{-2} or less, the mass loading of the active material $TPABr_3$ is about 40 mg cm^{-2}; in the battery cathode with a capacity of 10 mAh cm^{-2}, the mass loading of $TPABr_3$ is about 95 mg cm^{-2}; in the battery cathode with a capacity of 20 mAh cm^{-2}, the mass loading of $TPABr_3$ is about 200 mg cm^{-2}; in the battery cathode with a capacity of 50 mAh cm^{-2}, the mass loading of $TPABr_3$ is about 600 mg cm^{-2}.

The $Zn-Br_2$ pouch cell used a 6×6 cm^2 carbon felt loaded with $TPABr_3$ as the cathode, a 6×6 cm^2 brass with pre-deposited Zn as the anode, a 7×7 cm^2 glass fiber as the separator, and 10 mL of 0.5 M $ZnBr_2$ + 0.25 M TPABr solution as the electrolyte. Meanwhile, a 2×11 cm^2 Ti foil was adhered to the cathode as current collector, while the size of the tab was 2×5 cm^2. The Zn anode tab was formed by extending the same size (2×5 cm^2) of the brass foil during the cutting. The laminating process was performed manually, and the cathode and anode were placed on opposite sides of the separator, with a 0.5 cm offset from the separator edges to ensure electrode alignment. The battery was secured with insulating tape to prevent movement. The assembly was then encapsulated in aluminum-plastic film, leaving an electrolyte injection port at the upper corner of one tab. After injecting the electrolyte via syringe, the pouch cell was gently pressed between two glass plates to eliminate air bubbles. Finally, the injection port was sealed to complete the pouch cell assembly. For electrochemical testing, the pouch cell was sandwiched between two 7×7 cm^2 rigid acrylic plates and clamped evenly on both sides using binder clips. The high stiffness of the acrylic plates enabled

uniform pressure distribution across the entire electrode area, ensuring consistent interfacial contact during measurements. Among them, the cathode is loaded with about 2.1 g of $TPABr_3$, and the brass anode was pre-deposited with Zn with a capacity of 6.7 mAh cm^{-2}. 1000 mAh pouch cell was assembled by stacking three sets of electrode sheets, which loading of the cathode was further increased to 3.5 g of $TPABr_3$.

Electrochemical tests

Galvanostatic charge-discharge measurements were performed on a battery testing system (Neware, Shenzhen). For half cells, constant-current charging was conducted to predefined capacities followed by discharge termination at a cutoff potential of -0.2 V. $Zn-Br_2$ batteries were charged via a constant-current and constant-voltage protocol (first charged to 2 V at a constant current, and then charged to specified capacity at a constant voltage of 2 V) and then discharged to 0.5 V at the same current. Electrochemical analyses, including Tafel plots, cyclic voltammetry (CV), linear sweep voltammetry (LSV), chronoamperometry (CA) and electrochemical impedance spectroscopy (EIS) were carried out using an electrochemical workstation (CHI 608E, Shanghai). Tafel and LSV plots were conducted in three-electrode system, while CA, CV and EIS were conducted in coin half-cells. The substrate stability measurements include HER overpotential and Tafel curves were conducted in the three-electrode systems, where the Cu and brass as working electrode, Pt foil as the counter electrode, and Ag/AgCl as the reference electrode. The electrolyte was select 2 M Na_2SO_4 to avoid the influence of Zn plating/stripping on the stability of substrate. Tafel curves were acquired at a sweep rate of 5 mV s^{-1} within a ±0.3 V window relative to the open-circuit potential. In addition, the Tafel curve test was started after about 30 min of OCP monitoring prior to the test and the voltage variation was less than 5 mV per minute. LSV profiles were recorded from -1.0 to -2.0 V (vs. SHE) at 5 mV s^{-1}. The CV curves for testing the Zn deposition behavior were conducted at a scan rate of 5 mV s^{-1} and a range of -0.3 to 0.1 V vs. Zn^{2+}/Zn. Additionally, the CV curves for testing the stripping behavior of the Zn component in the brass substrate were measured at a scanning rate of 1 mV s^{-1} and in the range of 0 to 1.2 V vs. Zn^{2+}/Zn. The CA curves were maintained

at a potential of 85 mV for 1000 s. EIS measurements employed 5 mV amplitude with frequency scanning from 0.1 ~ 100 kHz. All experiments were conducted under room conditions (~25 °C).

Simulation and calculation details

The electrochemical behavior and mass transport dynamics during Zn deposition were numerically investigated through a multiphysics coupling approach in COMSOL Multiphysics. The simulation framework integrated the Secondary Current Distribution module with the Transport of Diluted Species interface to resolve interfacial reaction kinetics and ionic concentration gradients. A baseline electrolyte composition of 2 M ZnSO$_4$ aqueous solution was established as the initial condition.

In the simulations of Zn plating, variation in surface energy, defined by a stochastic function and manifested as $\Delta\gamma$ fluctuating between 0.9~1.1 γ (γ represents surface energy), induces fluctuations in the exchange current density. This promotes preferential nucleation at sites with lower surface energy.

Electrode kinetics are modeled by a modified Butler-Volmer equation (Equation 1) coupling surface energy disparities (γ represents surface energy, $\Delta\gamma$ is variation (0.9~1.1 γ), α is transfer coefficients, F/RT is the Nernst parameter, k_B is the Boltzmann constant, and T is the temperature) to electrochemical reaction rates. Following Zn deposition gradually cover the substrate surface, these surface energy variations gradually diminish, facilitating a relatively uniform electric field distribution while maintaining uniformity during prolonged Zn deposition. Moreover, the deposition morphology is statistically derived from mathematical models, which generally represents a uniform plated Zn distribution.

$$j = j_0 \left[exp\left(\frac{\alpha F\eta}{RT}\right) - exp\left(-\frac{(1-\alpha)F\eta}{RT}\right) \right] \cdot exp\left(-\frac{\gamma\Delta\gamma}{k_B T}\right)$$

(Equation 1)

Furthermore, the initial energy landscape (e.g., local surface energy, current density and ion flux distribution) established by the brass substrate propagates through the growing Zn layer. This is modeled via time-inherited boundary conditions (Equation 2). The growth morphologies of Zn deposition in the simulation model

emerge from statistical sampling of the computational ensemble.

$$\nabla[\eta(x,y,t=0)] \rightarrow \nabla[\eta(x,y,t)]$$ (Equation 2)

Transient simulations spanning 500 s were executed to capture the spatiotemporal evolution of current density distributions and Zn ion flux patterns, with solution data sampled at 5 s intervals. The physical parameters were shown in Table S1. The Zn^{2+} concentration is set to 2 mol L^{-1}, which is consistent with the 2 M $ZnSO_4$ electrolyte used in experimental of Zn plating. Zn density and molar mass are intrinsic properties of metallic Zn, which is directly retrieved from standard references and input into the model. The simulation temperature is fixed at 25 °C, mirroring experimental conditions. Diffusion coefficients for Zn^{2+}, SO_4^{2-}, H^+, and OH^- ions, along with the equilibrium potential of Zn, are inherent parameters obtained from tabulated data in the CRC Handbook of Chemistry and Physics. An applied current density of 10 mA cm^{-2} is implemented, aligning with values commonly used in the literature and throughout this work. The ground potential is defined as 0 V in accordance with simulation conventions and electrical engineering standards.

The adsorption behavior of H atoms on the (101) surfaces of Zn, Cu and brass were investigated using density functional theory (DFT) calculations within the $Dmol^3$ module of Materials Studio. The Perdew-Burke-Ernzerhof (PBE) functional under the generalized gradient approximation (GGA) framework was employed for exchange-correlation interactions. A plane-wave basis set cutoff energy of 500 eV was utilized. Structural relaxations were proceeded until atomic forces and total energy changes fell below 0.02 eV/Å and 1×10^{-5} eV, respectively. To model the H-substrate interaction, slabs cleaved from the respective bulk crystals were employed, incorporating a vacuum layer exceeding 10 Å along the surface normal direction. To systematically evaluate H adsorption strength on Zn, Cu and brass (101) surfaces, two distinct high-symmetry sites, namely hollow and bridge positions, were considered for H atom placement. In order to evaluate the interaction between H atoms and the slab, the adsorption energy (E_a) was calculated as follows:

$$E_a = E_{total} - \frac{1}{2} \times E_{H_2} - E_{surface}$$ (Equation 3)

where E_{H_2} represents the energy of gas H_2, and $E_{surface}$ and E_{total} are the energy of the compound before and after binding H. Calculations were conducted in a vacuum environment, and the E_a is interpreted in the context of HER under standard electrochemical conditions (pH=0). This approach allows relative comparisons of E_a to evaluate the strategy's effectiveness in suppressing HER across a wide pH range of electrolytes, as relevant to Zn battery applications.

Calculation of the energy density and power density

The energy and power densities were calculated based on active materials in a Zn-Br_2 battery with an areal capacity of 5 mAh cm^{-2}. The active area of the electrode was 1 cm^2 with an active bromine cathode (TPABr$_3$) loading of ~40 mg. The Zn anode used a brass foil current collector with pre-plated active Zn of ~7.5 mg. At a current density of 50 mA cm^{-2}, the total discharge energy of the battery was ~7.3 mWh and a discharge voltage of ~1.47 V (Fig. S27). Thus, the calculated energy power densities were ~154 Wh kg^{-1} and ~1554 W kg^{-1} based on active materials, respectively.

The practical energy density was obtained in an optimized Zn-Br_2 pouch cell, which was calculated based on the weight of the entire pouch cell including both active and inactive substances. The cathode had a size of about 6 cm × 6 cm, and the active bromine cathode (TPABr$_3$) loading was about 1.9 g. A brass substrate was used as the current collector for Zn anode, which was pre-plated with about 0.43 g of active Zn. A 0.5 mm thick glass fiber was employed as the separator, and the electrolyte was 0.5 M ZnBr$_2$ and 0.25 M TPABr. In the pouch cell, the weights of the cathode, anode, separator, electrolyte, and package were about 2.25 g, 1.38 g, 0.21 g, 3.38 g, and 0.27 g, respectively (Fig. S38). The total discharge energy of the pouch cell was ~ 457 mWh (Fig. S39). Therefore, the calculated practical energy density was about 61 Wh kg^{-1}.
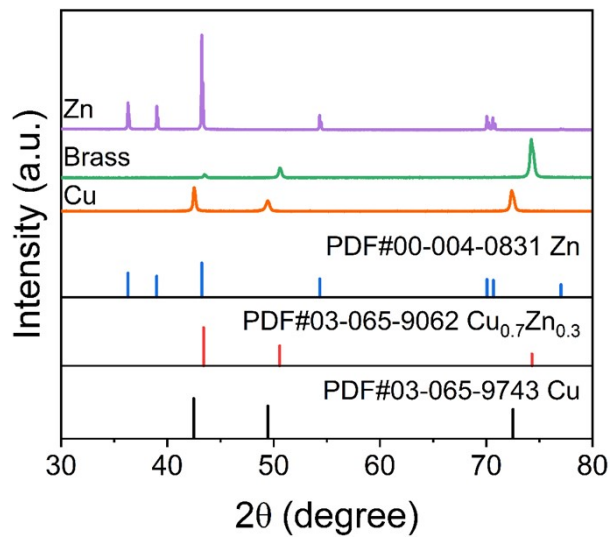
Fig. S1. XRD patterns of brass, Cu, and Zn substrates.
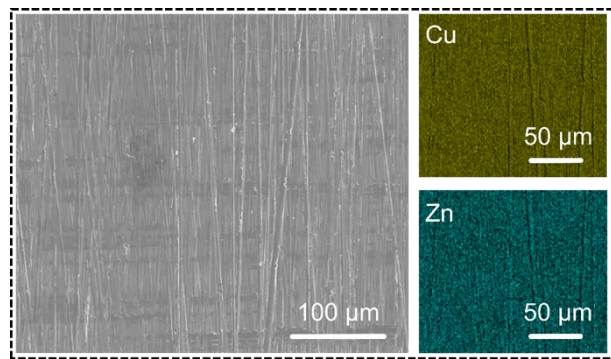
Fig. S2. SEM images and EDS elemental mapping of brass surfaces.
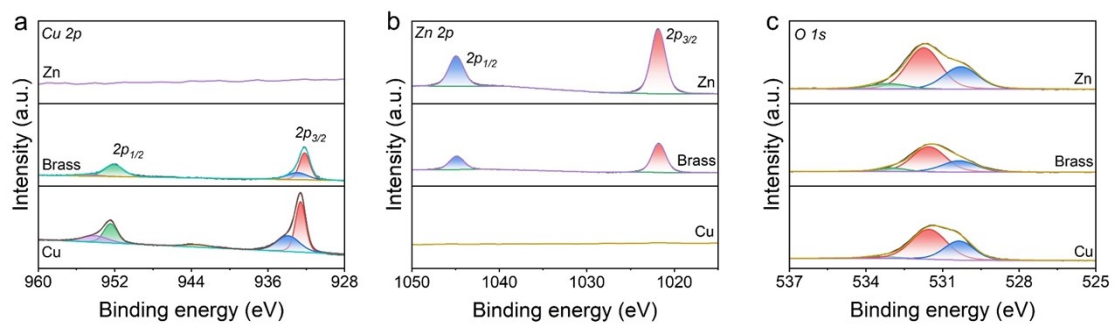
Fig. S3. XPS results of (a) Cu 2p, (b) Zn 2p, and (c) O 1s peaks on the surface of Zn, Cu, and brass substrates.
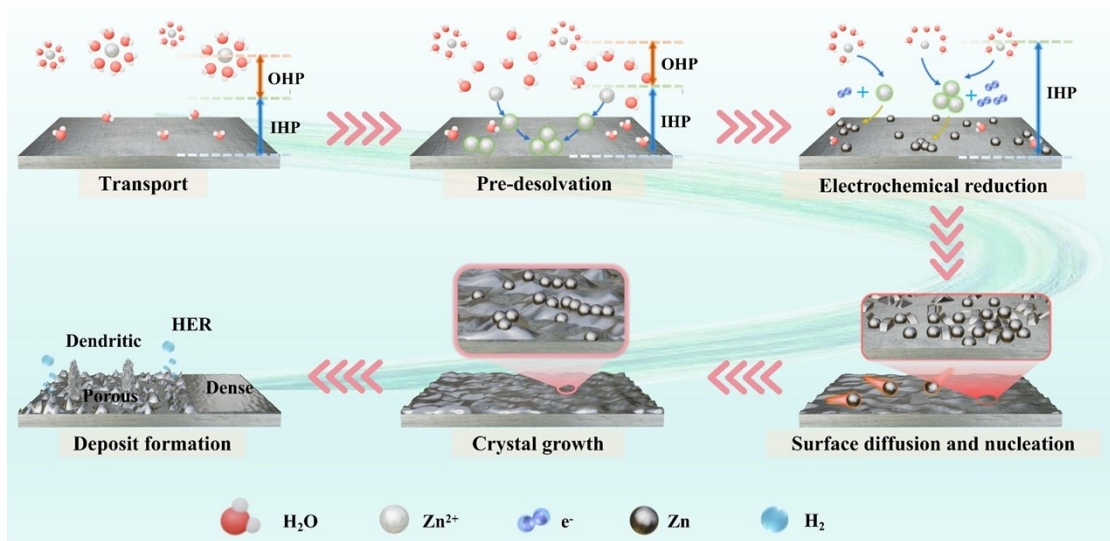
Fig. S4. Schematic diagram of the basic process of Zn electrodeposition.
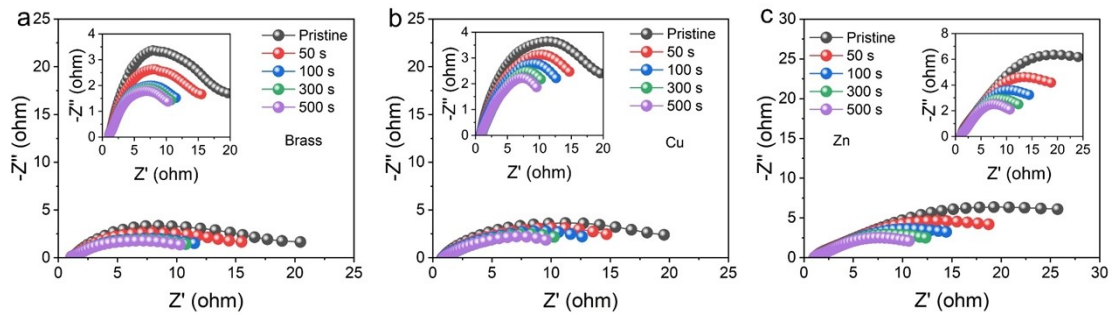
Fig. S5. The EIS curves of Zn|brass half-cells, Zn|Cu half-cells, and Zn|Zn half-cells with Zn deposition capacities ranging from 0 s to 500 s.
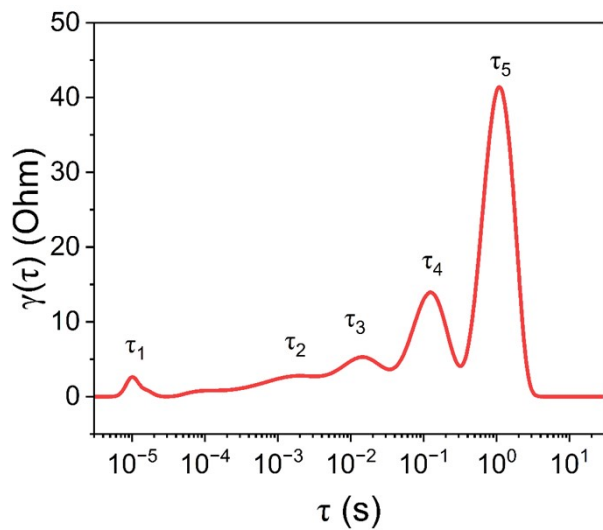
Fig. S6. The DRT plot of the pristine state of the Zn|brass half-cells.
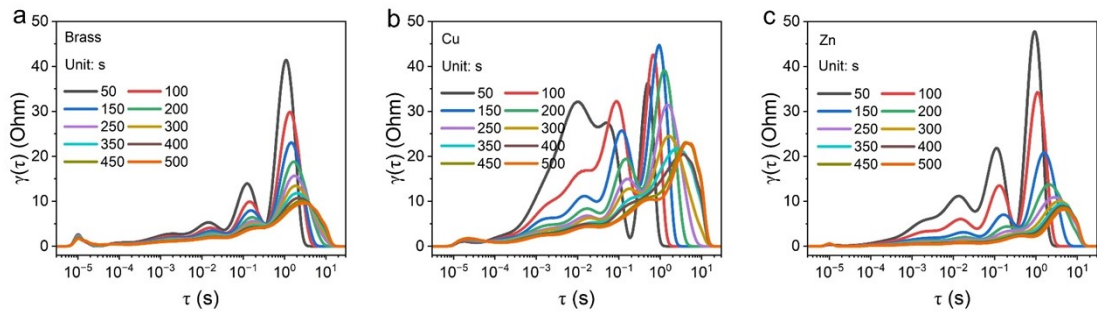
Fig. S7. The DRT plot during the Zn deposition process on (a) brass, (b) Cu, and (c) Zn substrates at a current density of 10 mA cm^{-2}.
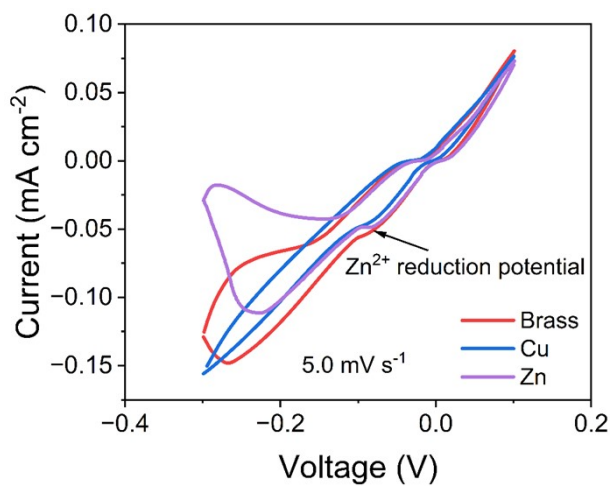
Fig. S8. The CV curves of Zn|brass half-cells, Zn|Cu half-cells and Zn|Zn half-cells at a scan rate of 5 mV s^{-1}.
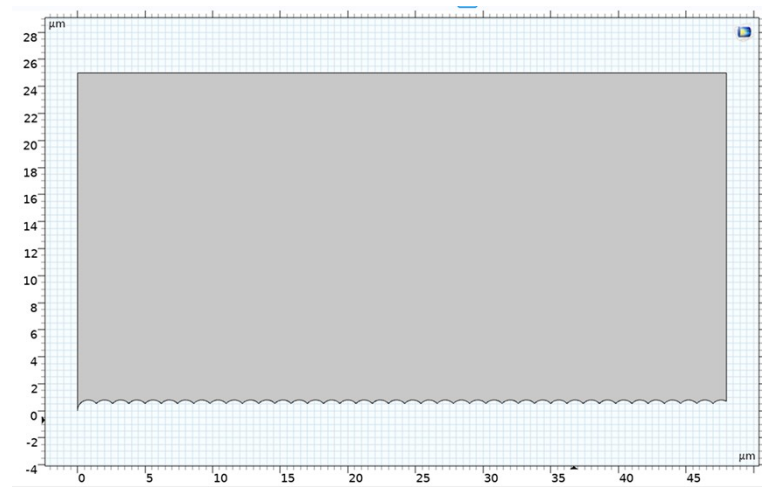
Fig. S9. Geometric model for COMSOL simulations.
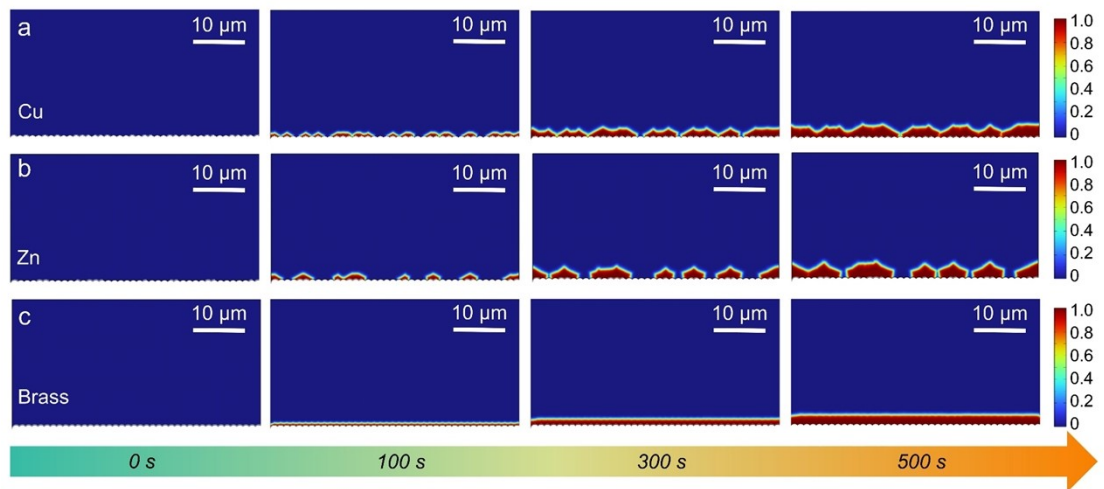
Fig. S10. COMSOL simulations of Zn deposition on different substrates. Zn deposition morphology on (a) Cu, (b) Zn and (c) brass substrates.
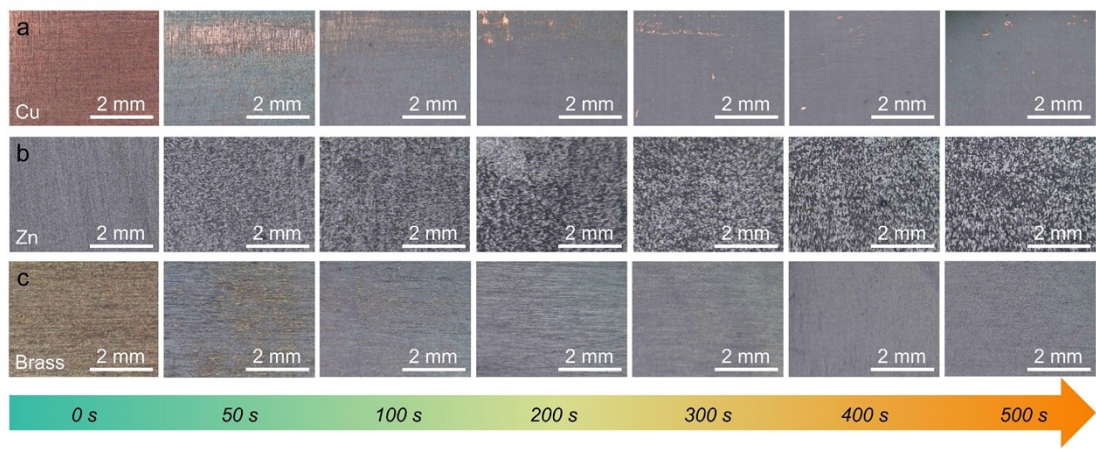
Fig. S11. Optical morphological observations of Zn deposition on (a) Cu, (b) Zn and (c) brass substrate at a current density of 10 mA cm^{-2}.
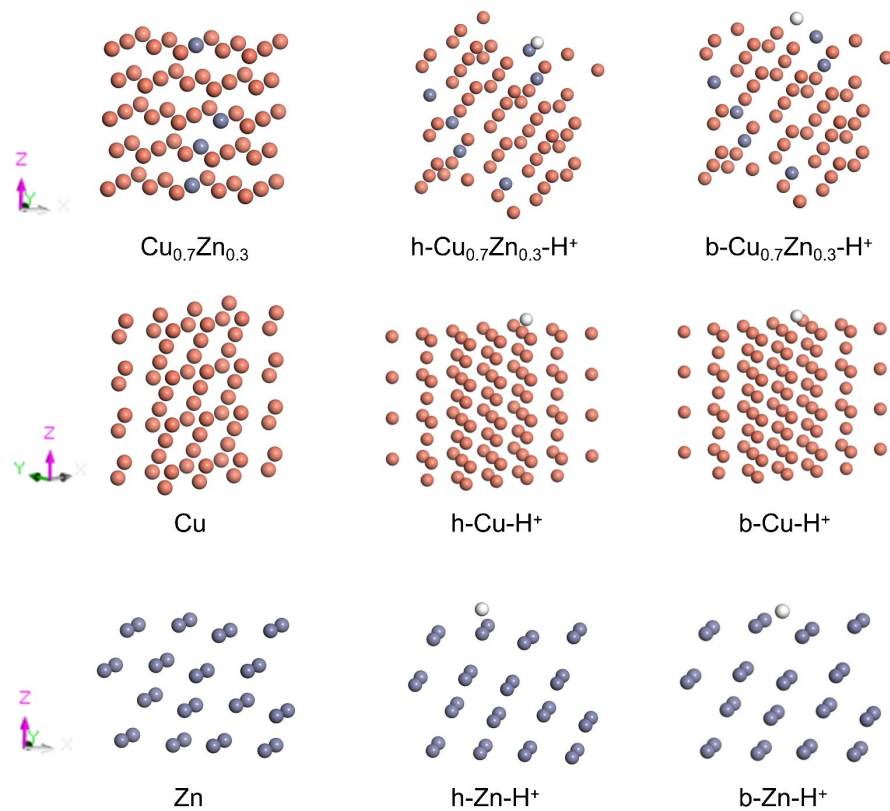
Fig. S12. Adsorption models of H^+ at different positions on brass, Cu and Zn substrates, where h represents the hollow position and b represents the bridge position.
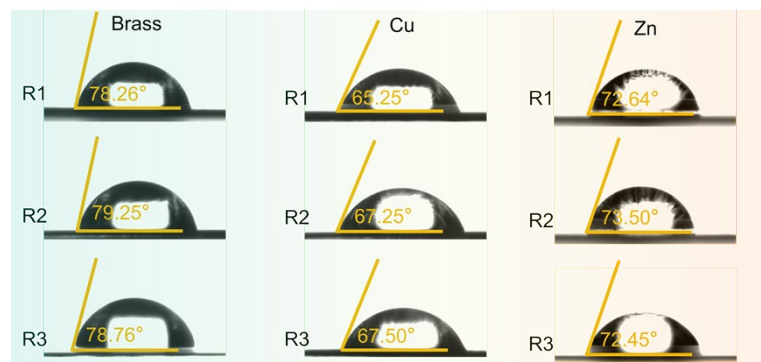
Fig. S13. The contact angle measurements at three different regions of 2 M $ZnSO_4$ electrolyte on brass, Cu and Zn substrates. "R" represents different regions.
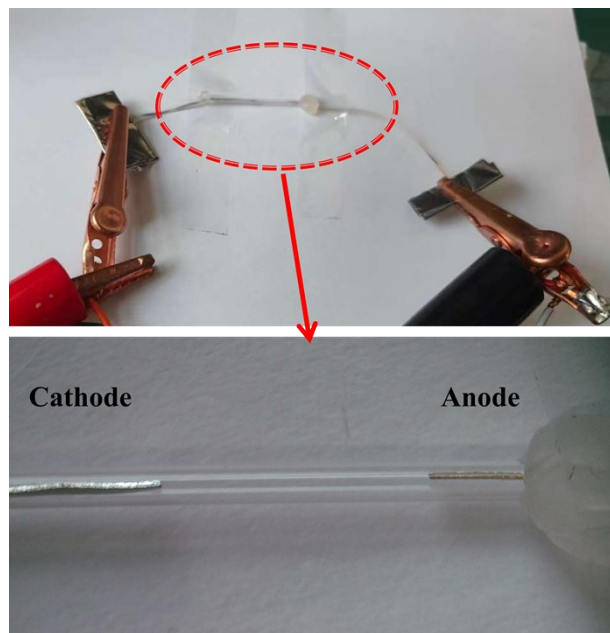
Fig. S14. The device for observing the HER behavior in a sealed glass fiber tube with a diameter of 0.9 mm.
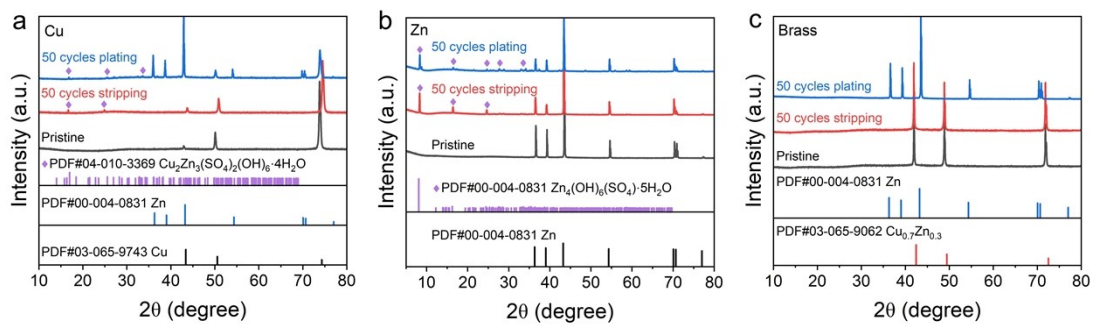
Fig. S15. XRD patterns of (a) Cu, (b) Zn and (c) brass after 50 cycles of Zn plating/stripping in 2 M ZnSO$_4$ electrolyte.
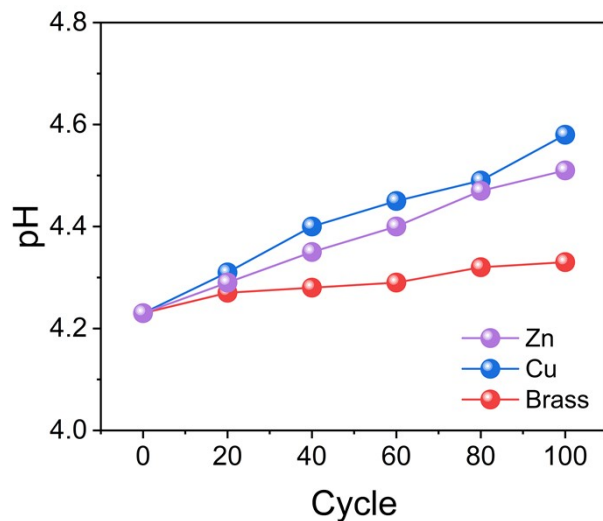
Fig. S16. The pH values of the electrolyte after different numbers of Zn deposition/stripping cycles on Cu and brass substrates in a 2 M ZnSO$_4$ electrolyte at an areal capacity of 10 mAh cm^{-2} and a current density of 10 mA cm^{-2}, respectively.
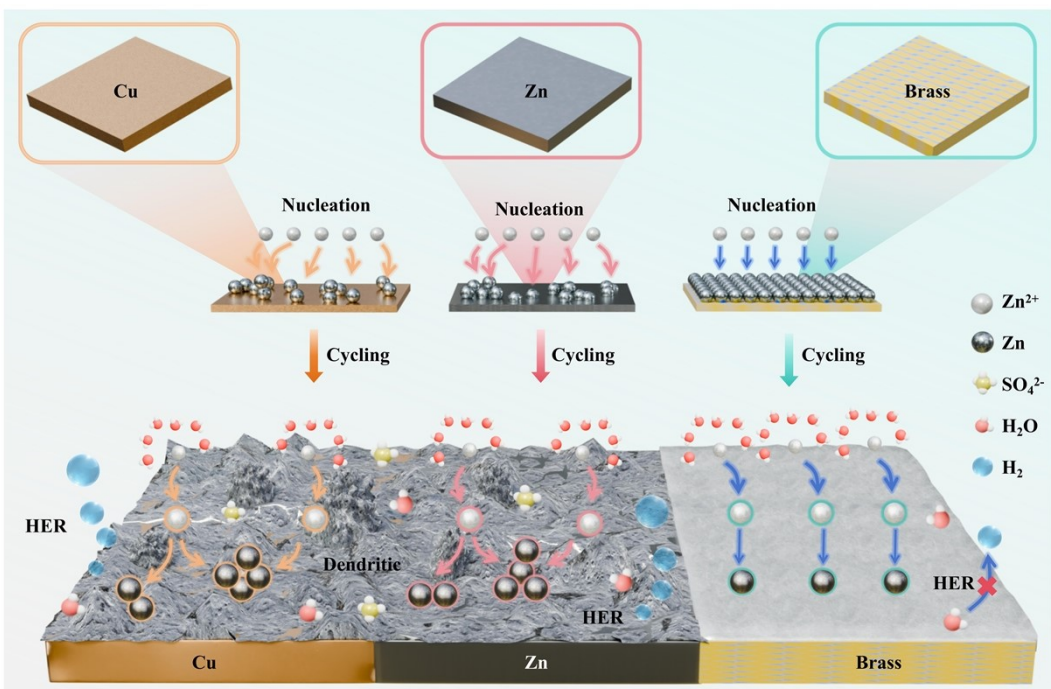
Fig. S17. Schematic illustration of Zn deposition mechanisms on Cu and Zn substrates with heterogeneous nucleation and brass substrates with restricted unfavorable reactions.
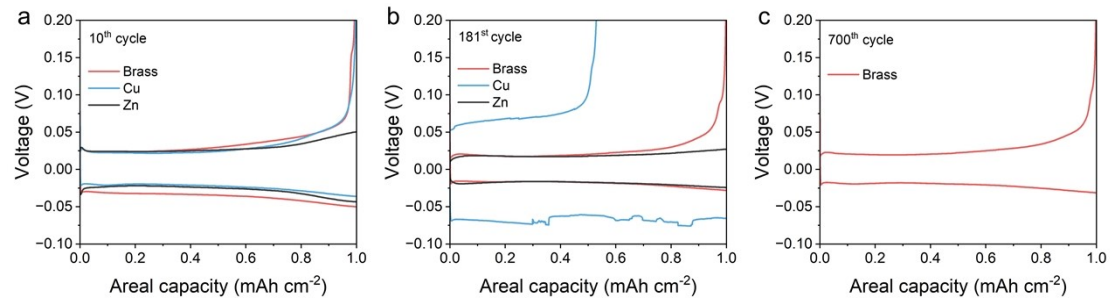
Fig. S18. Charge/discharge curves of Zn|Zn, Zn|Cu, and Zn|Brass half-cells at the (a) 10th, (b) 181st, and (c) 700th cycles under cycling conditions of 1 mAh cm^{-2} areal capacity with 1 mA cm^{-2} current density.
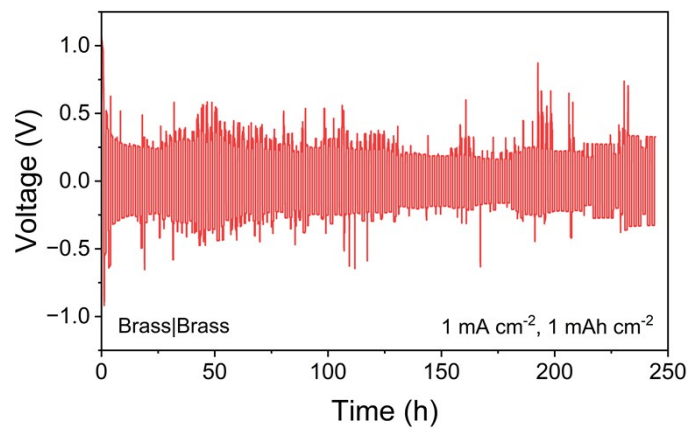
**Fig. S19.** Long cycling performance of Brass|Brass symmetric cell at 1 mAh cm^{-2} areal capacity with 1 mA cm^{-2} current density.
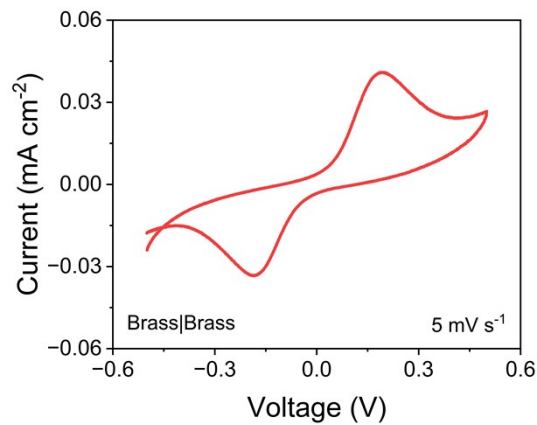
Fig. S20. The CV curves of Brass|Brass symmetric cell at a scan rate of 5 mV s^{-1}.
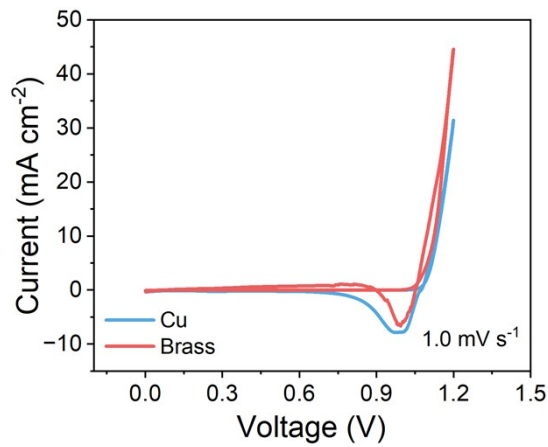
Fig. S21. CV curves of Zn|Cu half-cell and Zn|Brass half-cell at a scan rate of 1 mV s^{-1}.
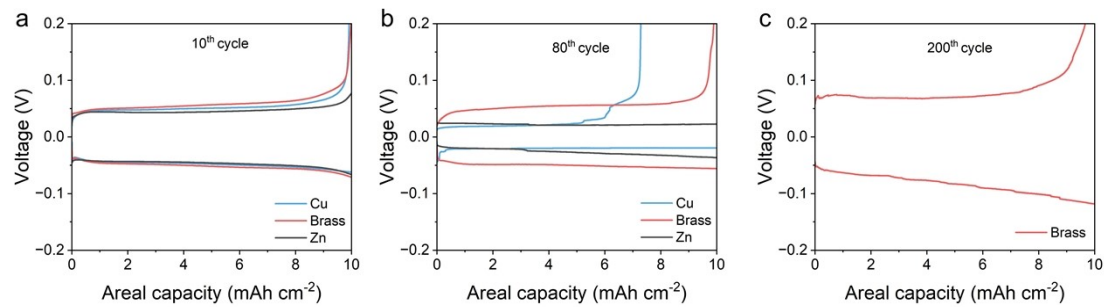
Fig. S22. Charge/discharge curves of Zn|Zn, Zn|Cu and Zn|Brass half-cells at the (a) 10th, (b) 80th, and (c) 200th cycles under cycling conditions of 10 mAh cm^{-2} areal capacity with 10 mA cm^{-2} current density.
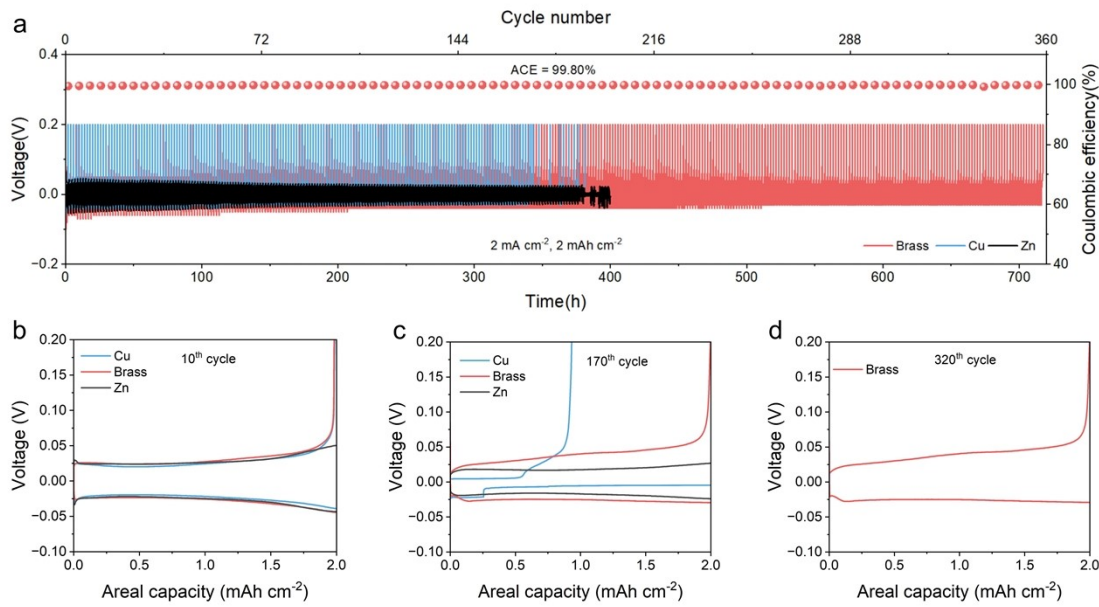
**Fig. S23.** (a) Long-term cycling performance of Zn|Zn, Zn|Cu and Zn|brass half-cells at 2 mAh cm^{-2} areal capacity with 2 mA cm^{-2} current density, and charge/discharge curves at (b) the 10th cycle, (c) the 171st cycle, and (d) the 320th cycle.
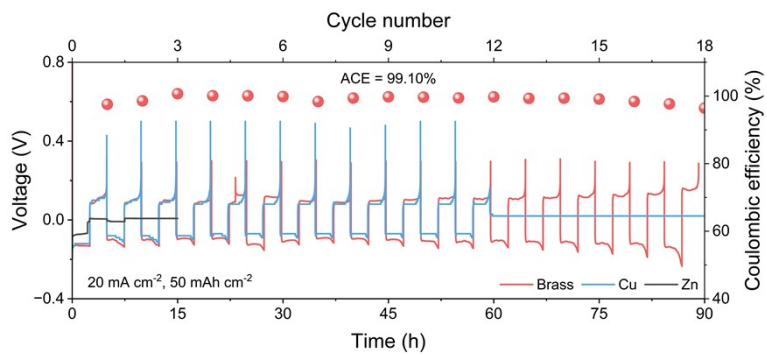
Fig. S24. Long-term cycling performance of Zn|Zn, Zn|Cu and Zn|brass half-cells at 50 mAh cm^{-2} areal capacity with 20 mA cm^{-2} current density.
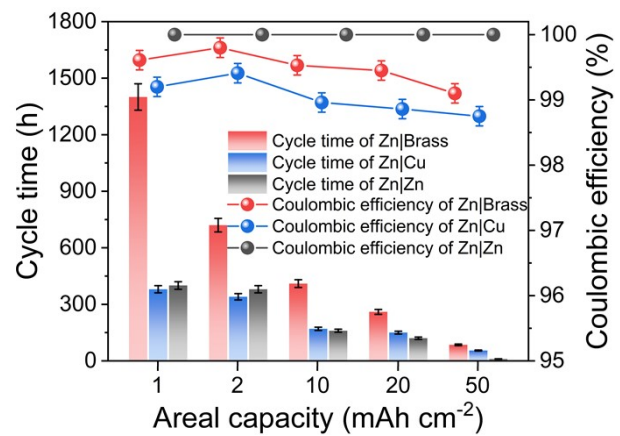
Fig. S25. Statistical chart of cycle time and average Coulombic efficiency of Zn|Zn, Zn|Cu and Zn|Brass half-cells at different areal capacities.
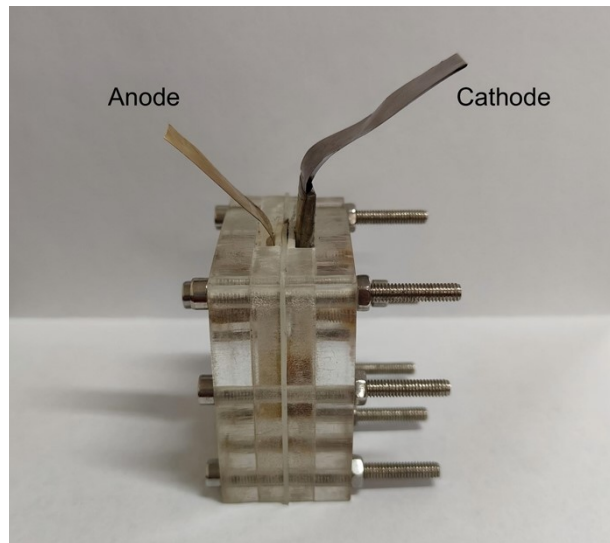
**Fig. S26.** The homemade plexiglass device for Zn-Br$_2$ battery tests.
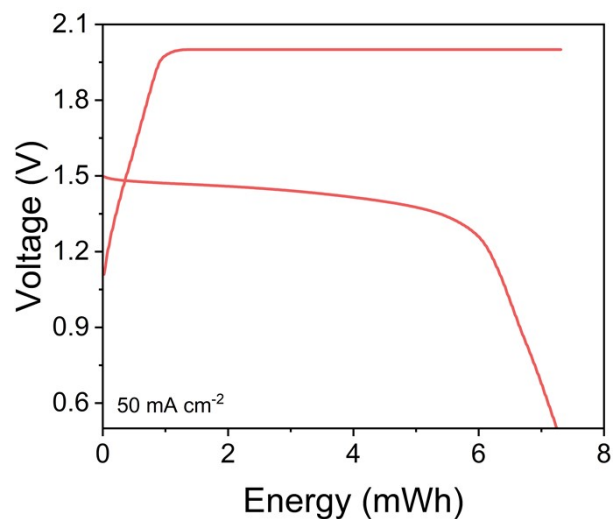
Fig. S27. Charge/discharge energy of the Zn-Br$_2$ battery at an areal capacity of 5 mAh cm^{-2} and a current density of 50 mA cm^{-2}.
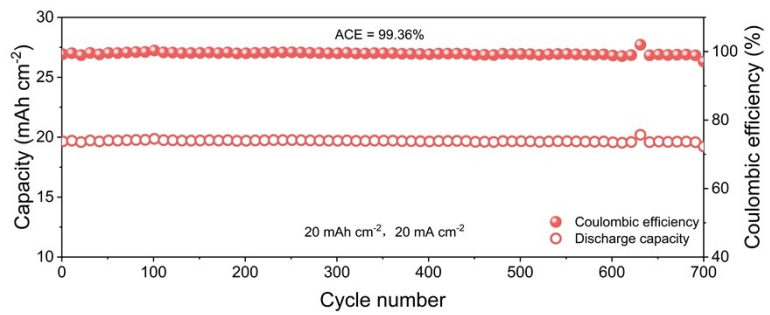
Fig. S28. Long-term cycling performance of Zn-Br$_2$ batteries at 20 mAh cm^{-2} areal capacity with 20 mA cm^{-2} current density.
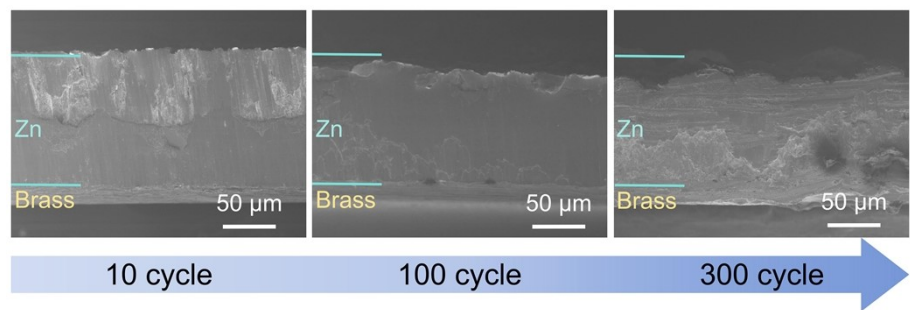
Fig. S29. Cross-sectional SEM images of the anode in Zn-Br$_2$ batteries with an areal capacity of 50 mAh cm^{-2} at different cycles.
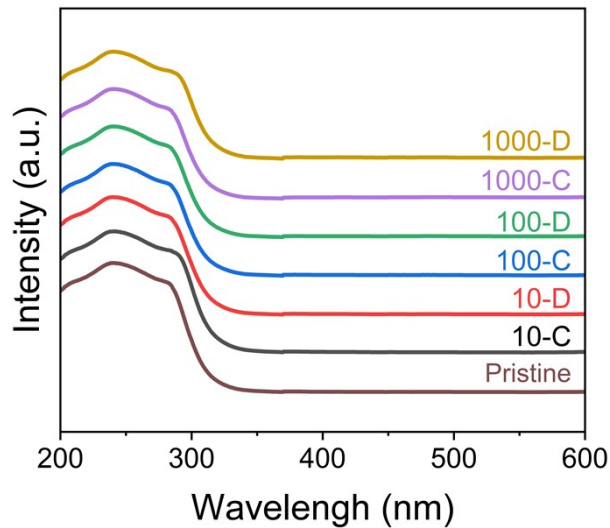
Fig. S30. The UV-vis spectra of the electrolytes in Zn-Br$_2$ batteries with an areal capacity of 1 mAh cm^{-2} at different cycles, where "C" and "D" represent charge and discharge states, respectively.
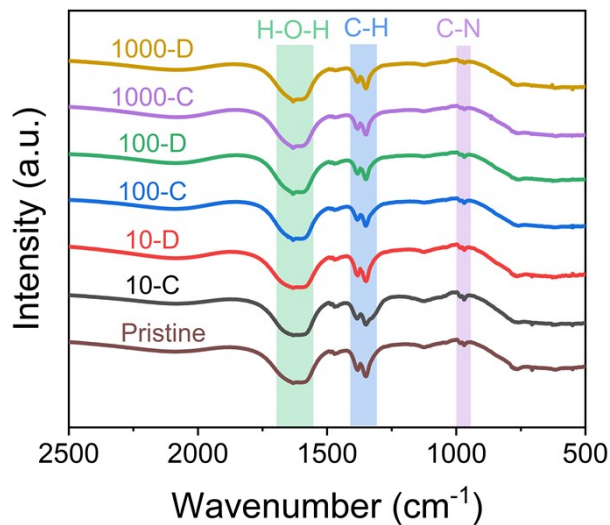
Fig. S31. The FT-IR spectra of the electrolytes in Zn-Br$_2$ batteries with an areal capacity of 1 mAh cm^{-2} at different cycles, where "C" and "D" represent charge and discharge states, respectively.
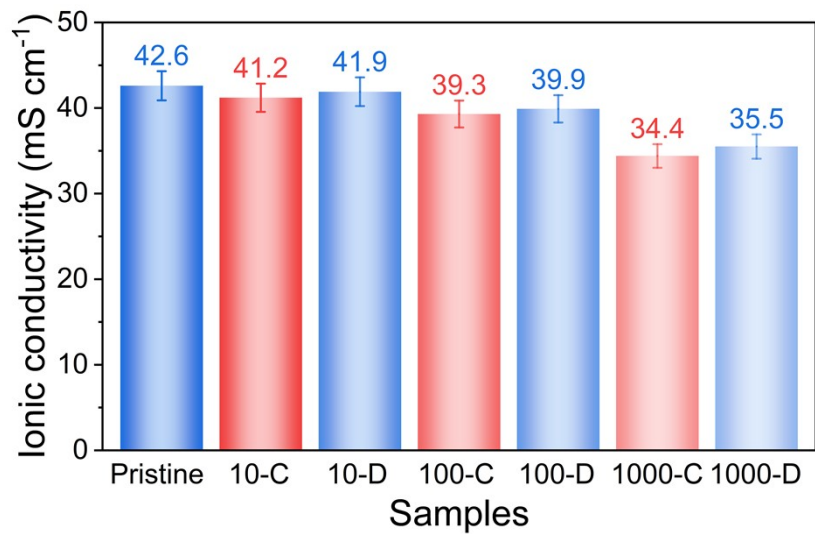
Fig. S32. The electrolyte ionic conductivity in Zn-Br$_2$ batteries with an areal capacity of 1 mAh cm^{-2} at different charge/discharge cycles, where "C" and "D" represent charge and discharge states, respectively.
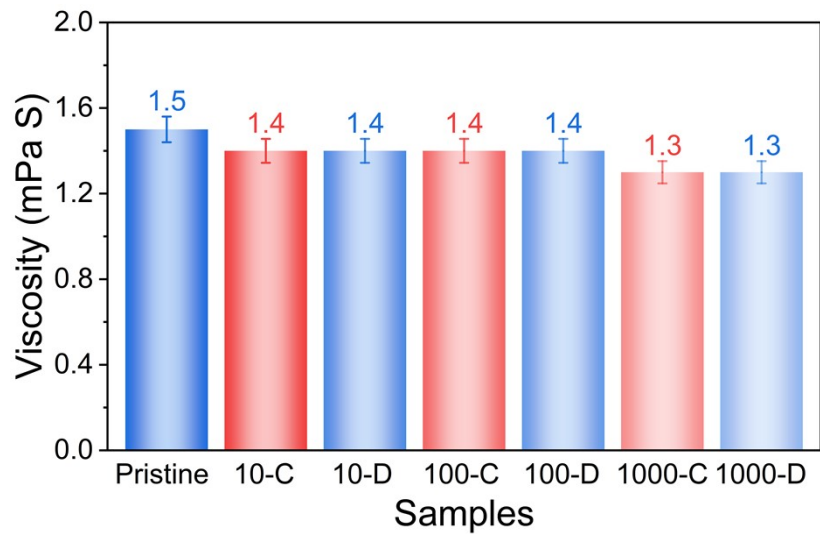
Fig. S33. The viscosity of the electrolyte in Zn-Br$_2$ batteries with an areal capacity of 1 mAh cm^{-2} at different charge/discharge cycles, where "C" and "D" represent charge and discharge states, respectively.
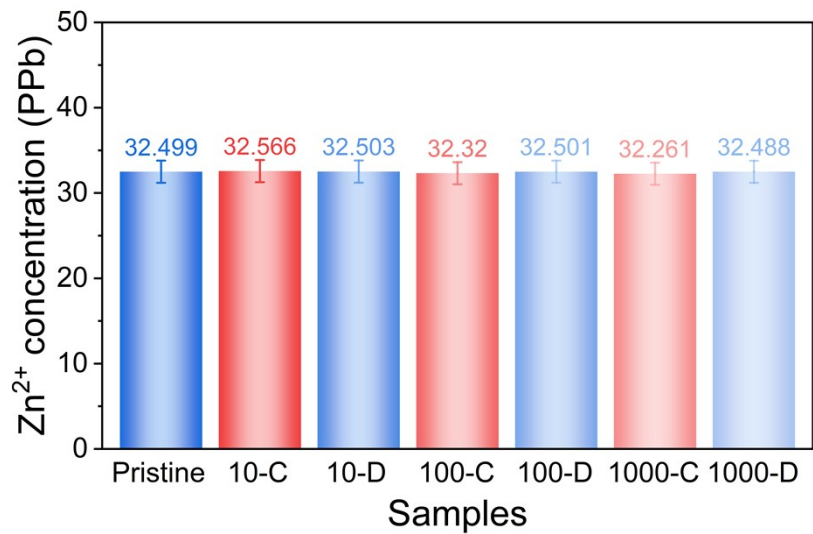
Fig. S34. The ICP-MS results of Zn^{2+} in the electrolytes of Zn-Br$_2$ batteries with an areal capacity of 1 mAh cm^{-2} at different cycles, where "C" and "D" represent charge and discharge states, respectively.
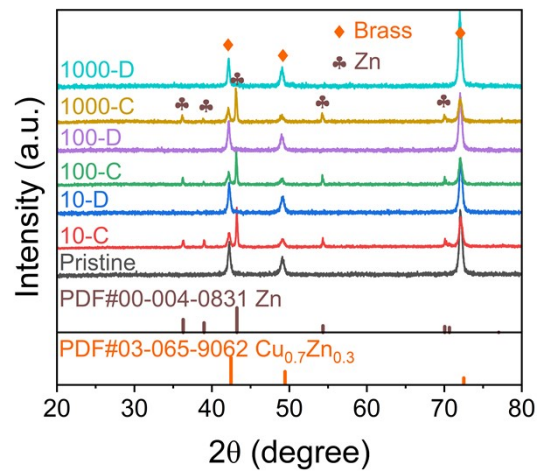
Fig. S35. The XRD patterns of the anodes in Zn-Br$_2$ batteries with an areal capacity of 1 mAh cm^{-2} at different charge/discharge cycles, where "C" and "D" represent charge and discharge states, respectively.
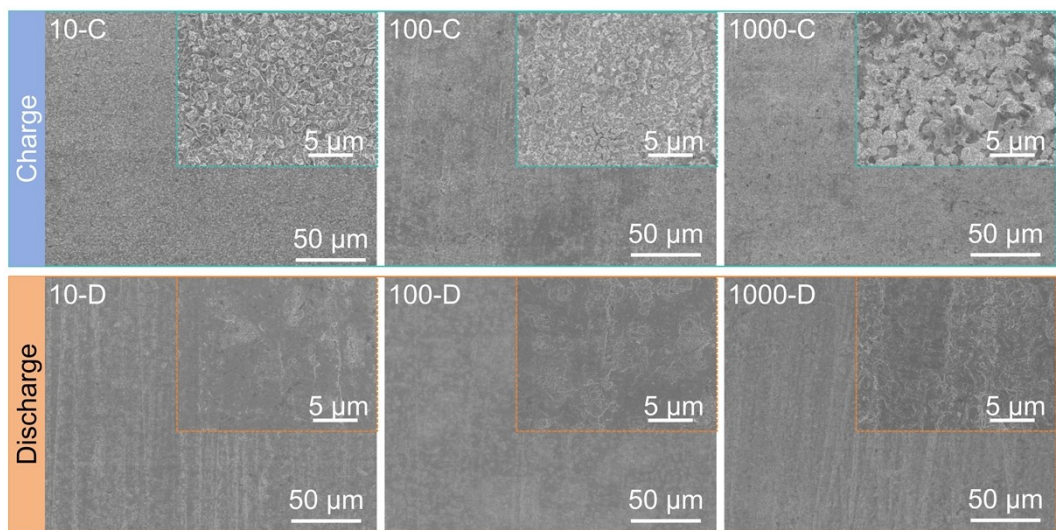
Fig. S36. The SEM images of the anodes in Zn-Br$_2$ batteries with an areal capacity of 1 mAh cm^{-2} at different charge/discharge cycles, where "C" and "D" represent charge and discharge states, respectively.
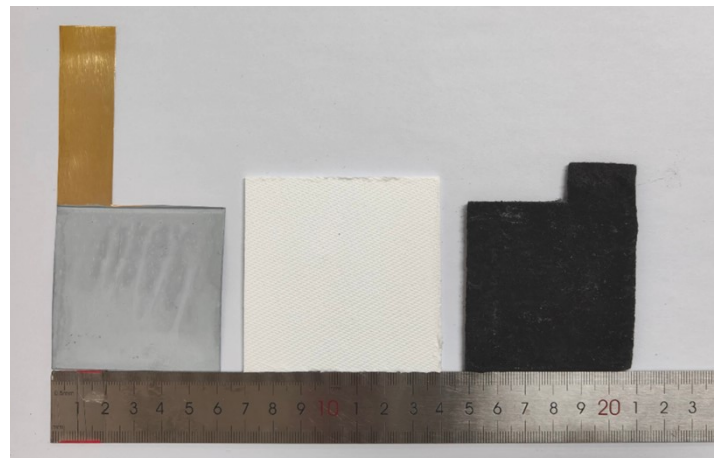
Fig. S37. Physical demonstration of 200 mAh capacity Zn-Br$_2$ pouch cell's electrodes, including TPABr$_3$@CF cathode, glass fiber, and Zn plated brass anode.

Fig. S38. Digital photo of the Zn-Br$_2$ pouch cell weighed on an analytical balance.
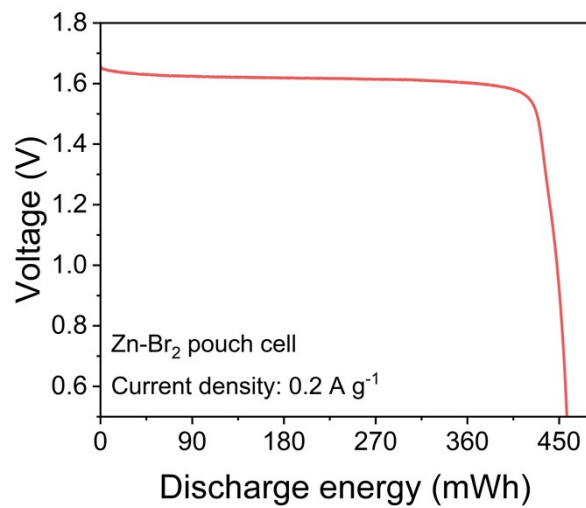
Fig. S39. Discharge energy of the optimized Zn-Br$_2$ pouch cell.
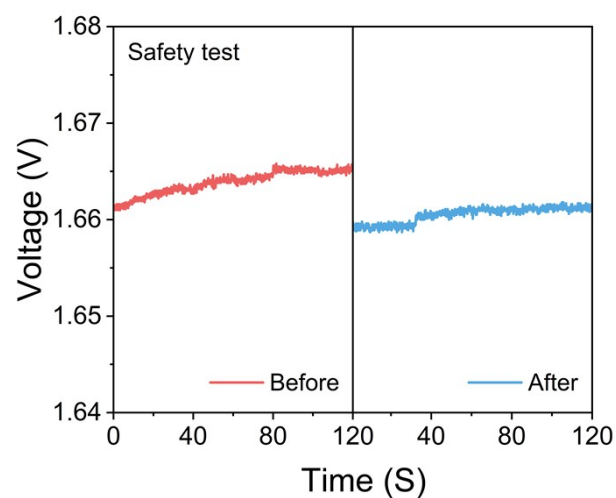
Fig. S40. The open-circuit voltage of Zn-Br$_2$ pouch cell before and after the safety test.
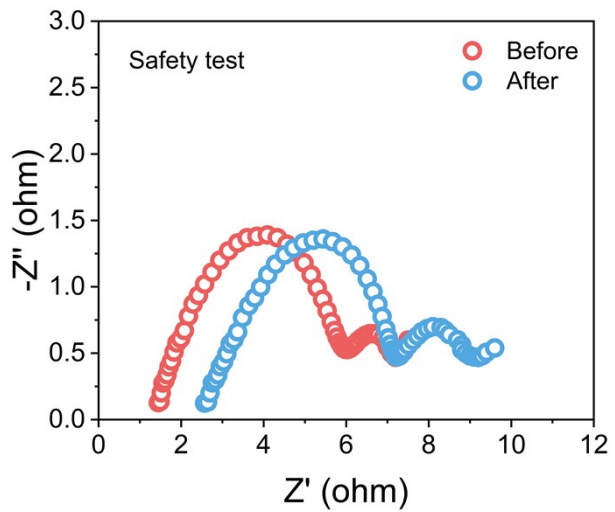
Fig. S41. The EIS of Zn-Br$_2$ pouch cell before and after the safety test.

Fig. S42. Simulation scenarios of smart grid applications for Zn-Br$_2$ battery applications.

Table S1. The physical parameters for COMSOL simulation.

Parameters	Values
Bulk concentration of Zn^{2+}	2 mol/L
Density of Zn	7140 kg/m³
Molar mass of Zn	0.06538 kg/mol
Temperature	293.15 K
Diffusion coefficient of Zn^{2+}	$0.712e^{-9}$ m^2 s^{-1}
Diffusion coefficient of SO_4^{2-}	$1.065e^{-9}$ m^2 s^{-1}
Diffusion coefficient of H^+	$9.3e^{-9}$ m^2 s^{-1}
Diffusion coefficient of OH^-	$5.3e^{-9}$ m^2 s^{-1}
Applied charge current density	10 mA cm^{-2}
Equilibrium potential	-0.76 V
Ground potential	0 V

Table S2. A summary of the electrochemical performance of Zn-based batteries in different systems.

Cathode (active material)	Mass loading (mg cm^{-2})	Areal capacity (mAh cm^{-2}) / Current density (mA cm^{-2})	Cycle number / Current density (mA cm^{-2}) / Areal capacity (mAh cm^{-2})	Energy density (Wh kg^{-1})	Power density (W kg^{-1})	Ref.
TPABr$_3$	40 - 600	5 / 50; 50 / 20	4800 / 10 / 5; 20000 / 10 / 1	154	1554	**This work**
BMIMBr	3 - 4	0.3 / 0.15; 0.15 / 3	3000 / 1 / 0.5	91	--	[1]
HPY Br	2.4 - 45	9 / 4.5; 2 / 10	1000 / 5.25 / 1.75	106	332.5	[2]
Oc$_4$NBr-KBr	5 - 22	1.35 / 1.35; 0.75 / 15	5000 / 11.25 / 1.125	--	2625	[3]
Br$_2$-solids	25	6.6 / 12.5; 2.25 / 75	1000 / 0.025 / 4.5	--	1700	[4]
IBr	2.07 - 13	0.553 / 4.14; 0.235 / 16.56	6000 / 4.14 / 0.403	385.8	3000	[5]
Ti$_2$CTx (Br$_2$)	2	0.2 / 1; 0.2 / 10	3000 / 1 / 0.2	--	--	[6]
TEABr$_3$	35	3 / 1; 3 / 24	1000 / 12 / 3	154	545.1	[7]
[bMImB]Br$_2$	10 - 45	4 / 2; 10 / 5	150 / 5 / 10	116	510	[8]
Sn/CNF (Br$_2$)	--	1.6 / 10	3000 / 10 / 1.6	--	--	[9]
a-MnBO$_x$	1.6	0.57 / 0.48; 0.12 / 32	10000 / 32 / 0.12	484.2	110.9	[10]
VO$_x$/MXene-x	1.5 - 2	336.39 mAh g^{-1} / 1 A g^{-1}; 213.06 mAh g^{-1} / 10 A g^{-1}	1000 / 10 A g^{-1} / 213.06 mAh g^{-1}	356.27	1280	[11]
A-VO$_x$@C/G	--	429 mAh g^{-1} / 0.5	2000 / 20 A g^{-1} / 315	321	381	[12]

A g^{-1}; 315 mAh g$^-$ mAh g^{-1}

^{1} / 20 A g^{-1}

References

1. R. H. Luo, X. H. Zheng, T. L. Jiang, D. Y. Shen, M. M. Wang, A. Mohsin, H. X. Liu, Z. D. Zhang, Y. C. Feng, H. Saba, P. Y. Tong and W. Chen, *Adv. Energy Mater.*, 2025, 2501658.

2. C. Xu, C. J. Lei, P. J. Jiang, W. Yang, W. J. Ma, X. He and X. Liang, *Joule*, 2024, **8**, 461-481.

3. X. Zhao, J. N. Hao, Q. R. Chen, S. J. Zhang, H. Wu, L. Mao and S. Z. Qiao, *Angew. Chem. Int. Ed.*, 2025, **64**, e202502386.

4. X. Y. Wang, Y. R. Ying, X. M. Li, S. M. Chen, G. W. Gao, H. T. Huang and L. T. Ma, *Energy Environ. Sci.*, 2023, **16**, 4572-4583.

5. S. M. Chen, Y. R. Ying, S. N. Wang, L. T. Ma, H. T. Huang, X. Q. Wang, X. Jin, S. C. Bai and C. Y. Zhi, *Angew. Chem. Int. Ed.*, 2023, **62**, e202301467.

6. J. J. Guo, G. L. Ma, G. Q. Liu, C. L. Dai and Z. F. Lin, *Adv. Energy Mater.*, 2024, **14**, 2304516.

7. S. S. Mollick, T. Mandal and S. Ramakrishnan, *J. Electrochem. Soc.*, 2025, **172**, 010503.

8. Y. T. Wu, C. Xu, C. J. Lei, W. J. Ma, W. Zhang, X. He and X. Liang, *Angew. Chem. Int. Ed.*, 2025, **64**, e202509293.

9. M. Rana, C. T. Stoppiello, Q. He, X. Y. Peng, N. Alghamdi, Y. X. Huang, I. R. Gentle and B. Luo, *Batteries Supercaps*, 2024, **7**, e202300474.

10. X. X. Li, C. C. Ji, J. K. Shen, J. Z. Feng, H. Y. Mi, Y. T. Xu, F. J. Guo and X. B. Yan, *Adv. Sci.*, 2023, **10**, 2205794.

11. J. Y. Sun, L. Zhang, F. B. Li, F. J. Yang, M. Y. Liu, S. B. Li and D. Q. Zhang, *Adv. Funct. Mater.*, 2025, **35**, 2501181.

12. R. Wang, H. H. Dai, T. Zhang, J. B. Zhou, L. A. Yin, J. Y. Zhou and G. Z. Sun, *Adv. Funct. Mater.*, 2025, **35**, 2421857.